The Astrophysical Journal, 754:102 (10pp), 2012 August 1 doi:10.1088/0004-637X/754/2/102

WHITE-LIGHT OBSERVATIONS OF SOLAR WIND TRANSIENTS AND COMPARISON WITH AUXILIARY DATA SETS

T. A. Howard[1], C. E. DeForest[1], and A. A. Reinard[2]
[1] Southwest Research Institute, 1050 Walnut Street, Suite 300, Boulder, CO 80302, USA; howard@boulder.swri.edu
[2] NOAA/SEC Mail Code W/NP92, 325 Broadway, Boulder, CO 80305, USA
Received 2012 April 19; accepted 2012 May 25; published 2012 July 13

ABSTRACT

This paper presents results utilizing a new data processing pipeline for *STEREO*/SECCHI. The pipeline is used to identify and track 24 large- and small-scale solar wind transients from the Sun out to 1 AU. This comparison was performed during a few weeks around the minimum at the end of Solar Cycle 23 and the start of Cycle 24 (2008 December to 2009 January). We use coronagraph data to identify features near the Sun, track them through HI-2A, and identify their signatures with in situ data at the Earth and *STEREO-B*. We provide measurements and preliminary analysis of the in situ signatures of these features near 1 AU. Along with the demonstration of the utility of heliospheric imagers for tracking even small-scale structures, we identify and discuss an important limitation in using geometric triangulation for determining three-dimensional properties.

Key words: methods: data analysis – solar–terrestrial relations – Sun: corona – Sun: coronal mass ejections (CMEs) – Sun: heliosphere

Online-only material: animations, color figures

1. INTRODUCTION

Heliospheric imagers provide information on the evolution of solar wind transient density structures across a large field of view (fov). It has been demonstrated that the current generation of heliospheric imager (HI; Eyles et al. 2009 and the now-deactived SMEI; Eyles et al. 2003) can identify and track large dense structures such as coronal mass ejections (CMEs; e.g., Howard et al. 2006; Harrison et al. 2008; Webb et al. 2009), corotating interaction regions (e.g., Sheeley et al. 2008; Rouillard et al. 2008; Tappin & Howard 2009a), and solar wind "puffs" (e.g., Rouillard et al. 2010) and "blobs" (e.g., Sheeley et al. 2009; Sheeley & Rouillard 2010). Heliospheric imagers bridge the gap between near-Sun measurements of transients (traditionally observed with coronagraphs) and their signatures near 1 AU. This has been attempted for CME observations in a number of publications (e.g., Tappin et al. 2004; Howard et al. 2006; Harrison et al. 2008; Davis et al. 2009; Möstl et al. 2010).

DeForest et al. (2011) describe the development of a new processing pipeline for *STEREO*/HI-2A, which is the heliospheric imager with the outermost fov (elongation range of 19°–89°) on the *STEREO* spacecraft that leads the Earth in its orbit about the Sun (*STEREO-A*). They showed that with this pipeline solar wind structures with surface brightnesses of the order of a few $\times 10^{-17}$ $B_\odot$ (where $B_\odot$ is the mean solar radiance of 2.3×10^7 Wm^{-2} sr^{-1}) can be identified and tracked out to large angles (>70°) from the Sun. They applied the pipeline on a 10 day data set in 2008 December and identified a number of features (including a CME) that were tracked to the Earth, allowing a comparison with in situ density measurements. In a following paper, DeForest et al. (2012) reported on a disconnection event observed during this time period and provided the first ongoing mass–time measurements of a transient using heliospheric imager data. They found that solar wind accretion occurred throughout the evolution of the disconnection event and found that the flux injected into the heliosphere by these events roughly balanced out that removed by CMEs. In a third paper, Howard & DeForest (2012a) focused on the observations of the CME and identified and tracked the magnetic cloud and sheath observed in situ back to their origins in coronagraph observations. They established that the magnetic cloud is the cavity component of the "classic" three-part CME structure (Illing & Hundhausen 1985) and measured the evolution of the structure of both the flux rope and the accompanying sheath.

DeForest et al. (2011) provide only a cursory examination of the features identified in the HI-2A data set, while DeForest et al. (2012) and Howard & DeForest (2012a) focus primarily on single events and related observations. In the present paper, we expand these works further by attempting a physical description of 24 solar wind transient structures observed throughout this time period by SECCHI-A. We use coronagraph observations to assign definitions to the structures, attempt their three-dimensional reconstruction using two independent techniques, and track them first through the coronagraphs, then HI-1A, HI-2A and finally, where possible, to their in situ signatures near 1 AU. We report on results of their tracking from the Sun to in situ impact, establishing similarities and discrepancies between features observed in white light and those observed in situ. Where possible, we identify the in situ signatures for particular smaller-scale solar wind transients. We conclude with a discussion on the reasons behind the discrepancy between the triangulation and TH results and alert the reader to a significant problem that arises from using triangulation calculations.

2. DATA

2.1. Selected Data Set

We examined integrated SECCHI data from *STEREO-A* over a 44 day window from 2008 December 9 through 2009 January 15. This time range encompasses the intervals of initial HI-2 analysis (DeForest et al. 2011) and CME tracking (Howard & DeForest 2012a). We selected this time range for two reasons:

1. The interval is near the end of Solar Cycle 23, during which time very low levels of solar wind activity were observed for an extended duration (e.g., Russell et al. 2010; Zita et al. 2010).

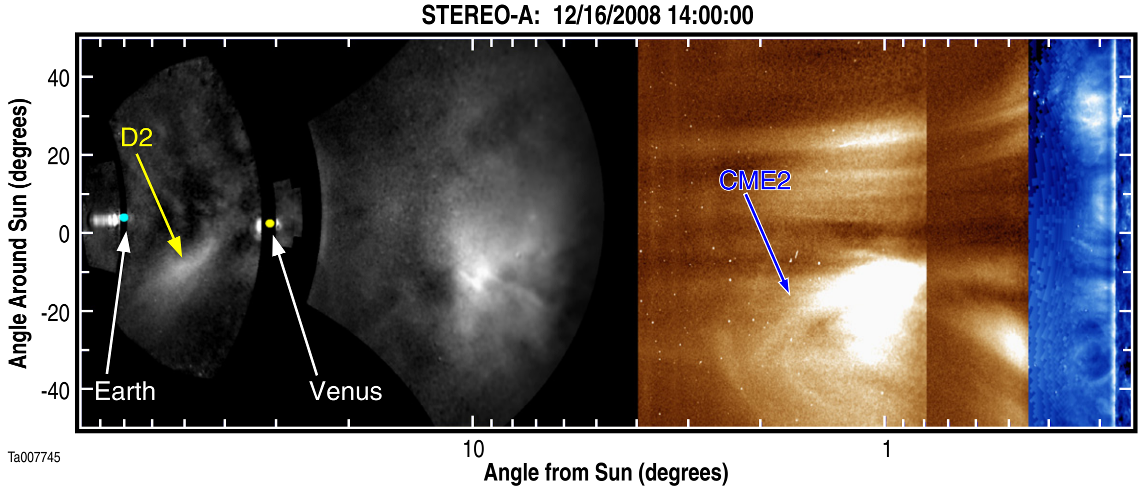

Figure 1. Combined SECCHI-A frame from the movie obtained on 2008 December 16 at 14 UT. The solar limb is in the EUVI image to the right (white vertical line); Earth and Venus are labeled. The fields of view from right to left are EUVI 171 Å (blue), CORs 1 and 2 (gold), and HIs 1 and 2 (gray). The units on both axes are in degrees: heliographic azimuth (y-axis) and solar elongation (x-axis), and the x-axis has been assigned a logarithmic scale. This projection is conformal, i.e., it preserves the shape of features that are small compared to their distance from the Sun. Two features (events) are labeled for comparison with Tables 1 and 2, and Figure 3.

(An animation and a color version of this figure are available in the online journal.)

2. An Earth-directed CME was launched on December 12, which turned out to be the first geoeffective CME clearly observed by *STEREO*. A number of papers have been published by other workers discussing this CME (Davis et al. 2009; Liu et al. 2010; Lugaz et al. 2010; Byrne et al. 2010). Two further CMEs occurred on January 7 and 8: these are discussed in more detail by Howard & DeForest (2012a).

We made use of data from SECCHI (Howard et al. 2008) on board *STEREO-A* and *STEREO-B*. During the selected time period, *STEREO-A* was ∼42° west of the Sun–Earth line at a radial distance of 0.97 AU from the Sun, and *STEREO-B* was ∼45° east of the Sun–Earth line at 1.03 AU from the Sun. The angular separation between both *STEREO* spacecraft was therefore ∼87°, i.e., near quadrature.

The Earth and *STEREO-B* appear in the *STEREO-A* fov, and they lie on the same azimuth as the ecliptic plane. Their elongations are identified using simple geometry:

$$\sin \varepsilon_A = \frac{r_0 \sin \alpha_0}{\sqrt{r_A^2 + r_0^2 - 2 r_A r_0 \cos \alpha_0}}, \quad (1)$$

where ε_A is the elongation relative to *STEREO-A*, r_0 and α_0 are the radial distance and azimuthal separation of the observed body, and r_A is the radial distance of *STEREO-A* from the Sun. From the vantage of *STEREO-A*, at the start of the year 2009 the Earth lay at a solar elongation of 70°.1 and *STEREO-B* was at 48°.6.

2.2. Processing

We processed the HI-2A data according to the procedure described by DeForest et al. (2011). Briefly, five major steps are applied to the data: stationary background removal, celestial background removal (including cross-image distortion measurement), residual F corona removal, moving-feature filtration in the Fourier plane, and conversion back to focal plane coordinates. The result is a sequence of images with the background stars and corona reduced by a factor between 10^3 and 10^4, revealing visible Thomson-scattered light. COR1, COR2, and HI-1 processing followed Howard & DeForest (2012a). Briefly, for HI-1 the polynomial fit step is performed in observing coordinates rather than celestial coordinates, and a simple F coronal subtraction was applied to the CORs.

Howard & DeForest (2012a) also describe the integration of the SECCHI movie showed in Figure 1. The movie has uniform cadence of 20 minutes, and each frame contains the closest-in-time data from each instrument in the SECCHI suite. The images have been normalized to approximately equal brightness variation across elongation, and the zero point of each pixel was selected based on a time-axis minimum scheme.

We include EUVI-A 171 Å data in the SECCHI data set for this work. EUVI data were minimally processed: beginning with the Level 0 data we found the average brightness value in the 15 × 15 pixel square in each corner of the 2048 × 2048 pixel image and averaged over all four values to find a "base pedestal value." This was subtracted from each pixel in the image.

2.3. Analysis

We have analyzed the white-light data (CORs, HIs) via two different means to identify three-dimensional structure of transients in the solar wind. In the first method, which was applied to the COR2 and HI-1 measurements, we use geometric triangulation via the method of Howard & Tappin (2008). That method applies geometry (derived from their Figure 3) to a number of points measured across the leading edge of the observed structure. The second method involves three-dimensional reconstruction on the leading edges of the solar wind features observed by the heliospheric imager HI-2A. We used the Tappin–Howard (TH) model (Tappin & Howard 2009b; Howard & Tappin 2010), which makes use of geometry to estimate the structure, trajectory, and kinematic evolution of any feature from which a leading edge measurement can be obtained. Because it takes advantage of the breakdown of geometrical simplicity that occurs at larger elongations (Howard & Tappin 2009; Howard 2011), TH is only effective with heliospheric imager data beyond around 20° of elongation.

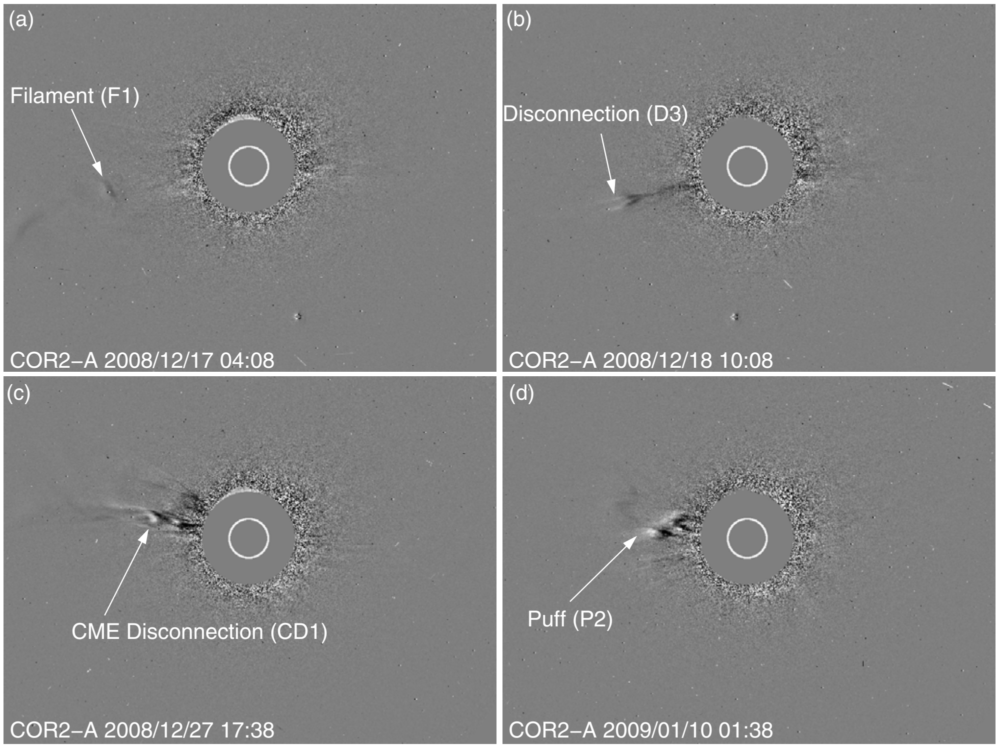

Figure 2. COR2-A running difference coronagraph images showing a selection of four events: (a) a filament (labeled F1 in Table 1), (b) a disconnection event (D3; the same as that discussed in detail by DeForest et al. 2012), (c) a CME disconnection event (CD1), and (d) a puff (P2). In each case the date and time are shown. The white circle near the center of the image represents the surface of the Sun and the gray solid disk is the occulting disk.

3. SUN AND INNER HELIOSPHERE AT SOLAR MINIMUM

Figure 1 is a frame from the integrated SECCHI movie with a number of features labeled in each frame. Large and small features stream from the Sun continuously throughout the movie and features can be tracked from the origins in the solar corona through the heliosphere. Many features can also be identified at large elongations (i.e., very large distances from the Sun). These results confirm two important properties of the solar wind: that even in the depths of solar minimum the solar wind is a dynamic medium heavily populated by transient phenomena; and that large and small solar wind disturbances created in the corona are present out to very large distances from the Sun, to 1 AU and beyond.

4. FEATURE IDENTIFICATION

DeForest et al. (2011) identified a number of features, assigned generic observational labels to many of them, and tracked them through the HI-2A fov toward the Earth. DeForest et al. (2012) focused on a disconnection event, and Howard & DeForest (2012a) focused on those features related to the CME eruptions, that is the magnetic clouds and sheaths. Here we attempt to assign physically meaningful terms to the solar wind transient features by using instruments that observe closer to the Sun. For direct comparison we use COR1-A, COR2-A, and HI-1A data, but we also compare features observed by COR1-B, COR2-B, LASCO, and the EUVIs.

For simplicity, we have selected 24 features (henceforth referred to as events) that range in size, structure, and origin. We selected them because they could be tracked unambiguously through the entire SECCHI-A fov, including HI-2. We have not attempted to identify and measure every observed feature; for example, DeForest et al. (2012) identified many more disconnection events than have been listed here because they did not impose a requirement to track each event continuously through all of SECCHI-A. The three-dimensional results for the 24 events, obtained from the two techniques, are summarized in Table 1. We have assigned a label and an attempt at a physical description to each, based on observations in the coronagraph data. This list includes five CMEs, three of which are discussed in more detail by Howard & DeForest (2012a), and the disconnection event discussed by DeForest et al. (2012).

Figure 2 shows selected coronagraph images with some of the events we have identified. We have attempted to assign a physically meaningful description based on documented observations by previous workers using coronagraph data. Those labeled "CME" are transients that appear to display the "classic" three part CME structure (leading bright front followed by a cavity followed by a trailing filament), although some did not display a clear filament signature. For those with a filament eruption we have measured that structure as well, and labeled them as "Filament" (F). In one case we have also measured the cavity of the CME. This is labeled as a "Void" (V) and has been studied in detail by Howard & DeForest (2012a). Many of the CME events were followed by an ejection that appeared to show a disconnection, perhaps of the CME itself from the coronal field. These have been labeled "CME disconnection" (CD). A solar wind "blob" is a term used to describe fragments of coronal material disconnected from the cusps of coronal streamers (Sheeley et al. 1997). While many of the events observed here did appear to originate from coronal streamers and seemed to match the appearance of the blobs described in the literature, most of them did not originate from the cusps of the streamers, and so we did not label them as blobs. Only one event appeared to match the description of a blob sufficiently, and we have labeled it as such (B). A number of events have also been labeled as "Disconnection" (D). These match the description of

Table 1
Observational Summary of the 24 Features Selected for Analysis Observed in the SECCHI Data Set of 2008 December to 2009 January

Label	Time 1st	Triangulation (°)			TH model						Physical
	App. (UT)	Λ	ΔΛ	Φ	ΔΦ	Λ	ΔΛ	Φ	ΔΦ	ρ	Description
	2008										
D1	12/11 0508	1.6	...	−72.1	...	−23.5	72.0	−23.9	18.4	−1.45	Disconnection
CME1A	12/12 0908	29.7	70.8	28.6	23.1	24.0	38.6	−12.3	56.0	2.13	CME (north)
CME1B	12/12 1038	−6.0	10.2	56.5	49.5	−9.2	24.0	−8.8	24.0	−0.10	CME (south)
V1	12/12 1108	61.1	52.8	37.9	26.5	24.0	30.9	−8.9	24.0	−1.21	Void
P1	12/13 0208	0.3	...	5.6	...	11.8	21.0	2.7	14.6	2.6	Puff
D2	12/13 0908	5.4	...	38.6	...	6.0	23.8	3.8	19.2	1.36	Disconnection
CME2	12/16 0938	−11.9	9.4	−34.3	31.6	−12.0	24.0	1.4	24.0	0.50	CME
F1	12/17 0138	−24.5	5.3	−39.5	2.1	29.7	24.0	−14.5	44.2	−0.28	Filament
D3	12/18 1038	−19.0	...	−17.7	...	−18.0	12.0	−4.5	14.4	−1.58	Disconnection
CME3A	12/27 0938	12.6	31.4	−60.5	37.2	−0.8	70.3	−69.3	117.3	−1.03	CME (leading)
F2	12/27 1008	3.5	9.8	−42.5	78.8	32.0	41.1	1.8	21.3	2.22	Filament
CME3B	12/27 1108	9.2	20.0	−94.1	34.3	−24.1	16.0	26.4	24.0	2.32	CME (trailing)
CD1	12/27 1138	7.8	13.1	−63.8	23.9	30.0	36.1	13.5	23.8	1.54	CME disconnection
D4	12/28 0408	2.2	...	−69.5	...	0.0	24.0	8.9	62.3	0.05	Disconnection
D5	12/28 1438	13.1	...	−6.3	...	36.0	24.0	−8.6	51.3	−1.00	Disconnection
B1	12/31 1708	1.4	...	−39.3	...	−24.0	12.0	−49.6	8.4	−1.82	Blob
	2009										
CME4	01/01 0038	0.1	14.9	6.2	22.2	−20.4	17.7	19.2	31.4	0.57	CME
CD2	01/01 1408	14.6	...	−10.6	...	38.6	43.5	17.6	33.3	1.72	CME disconnection
D6	01/05 1508	12.5	...	73.0	...	−30.0	36.1	−11.0	12.1	−2.42	Disconnection
CME5A	01/07 1638	0.7	5.7	−48.8	42.2	18.7	17.2	7.2	12.0	0.12	CME (leading)
CME5B	01/07 1708	−5.9	9.8	24.8	9.4	24.0	19.9	21.0	58.4	0.50	CME (trailing)
CD3	01/07 2308	0.8	...	−1.8	...	−11.8	45.8	1.4	12.3	−0.20	CME disconnection
CME6	01/09 0138	−1.8	22.0	−34.0	15.7	12.1	108.8	109.3	65.7	0.00	CME
P2	01/10 0138	1.2	16.6	31.3	56.7	15.5	116.5	95.6	98.4	0.38	Puff

Notes. A label has been assigned to each, and the location determined from the triangulation and TH model results are provided. Coordinates are latitude Λ, latitude width $\Delta\Lambda$, longitude Φ, and longitude width $\Delta\Phi$, are heliocentric–Earth–ecliptic, and the convention is positive = north and west. If a latitude and longitude width is not provided it is because the event was too narrow to obtain width measurements. The TH model also provides a distortion parameter ρ, which is included. The final column is an additional label that assigns what the authors believe to be a physically reasonable description for each event. The meaning of these descriptions is discussed in the text. Those events that are suspected to impact the Earth or one of the *STEREO* spacecraft (see Section 6) are highlighted in italic font.

flux disconnection events that have been described many works (e.g., McComas et al. 1991, 1992; Linker et al. 1992) and are discussed in further detail by DeForest et al. (2012). Finally, two events did not match any of the descriptions provided above but could still be unambiguously tracked throughout SECCHI-A. This includes features that were similar in appearance as blobs but were not associated with the cusps of streamers. We have labeled these simply as solar wind "Puffs" (P). These physical classifications are based primarily on white-light morphology and therefore constitute a descriptive mode of each event, rather than a direct observation.

During the selected 44 day time period we have identified 5 CMEs, 2 filaments, 1 void, 3 CME disconnections, 1 blob, 6 disconnections, and 2 puffs. Along with their location we have elongation measurements at different times and so we can identify the radial distance of each event at all times as well as their latitude, longitude, and spatial extent. Elongation has been converted to distance using the Point-P approximation (Houminer & Hewish 1972; Howard et al. 2006) for observations in COR1, COR2, and HI-1, and using TH for observations in HI-2. TH also provides a distortion parameter ρ which is an indication of the curvature of the CME. The meaning of ρ is described by Howard & Tappin (2010) as a variation of the standard spherical shell (or cone). A value of $\rho = 0$ is the spherical shell, values greater than 0 indicate a more strongly curved or bubble-like structure, -1 indicates a flat shape, while values less than -1 indicate a structure that is concave outward (i.e., pointing toward from the Sun). The TH results reveal five events that are concave outward, including the CME void (V1).

5. LOCATION AND KINEMATIC EVOLUTION

Using the location results from Table 1 and the radial distances, we may assign a location in three-dimensional space for every event at all times at which measurements were made. Figure 3 shows selected frames from a movie showing the location of the events throughout the data set. The times have been normalized to an hourly cadence. (The complete movie is available in the online version of this paper.) Two projections of these events are shown: looking down from north onto the ecliptic plane, and a meridional view showing the projected location onto the surface of the Sun. Onto the latter we have added approximate locations of the streamer belt (green curves) surrounding the heliospheric current sheet, determined using measurements of the northern and southern edges of the streamer belt as observed by COR2-A and COR2-B.

Inspection of the extracted feature location movie reveals four immediate results. Triangulation and the TH model show great variation in their level of agreement. For many events the triangulation results place the event further from the Sun–Earth line than the TH results do. A possible reason for this is discussed in Section 7.1.1. For other events, the three-dimensional analysis place a feature outside the SECCHI-A fov, such as the triangulation results of CME3B and D4 or the TH results of CME6 and

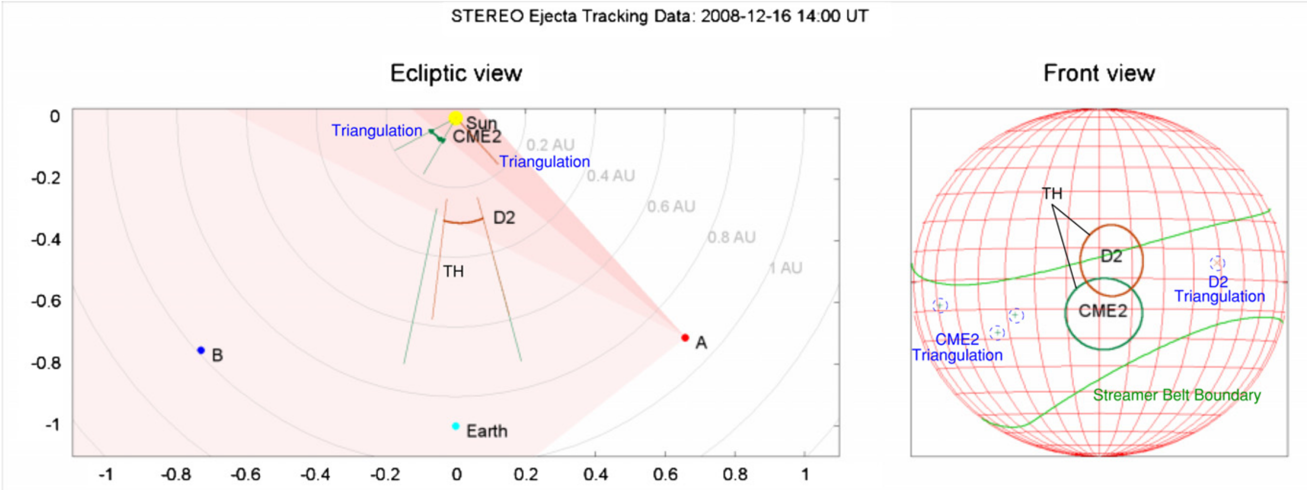

Figure 3. One frame from the reconstruction results, showing two events (CME2 and D2). For comparison, we have chosen the same time as the image in Figure 1: 2008 December 16 at 14 UT. Events have been labeled to correspond with Tables 1 and 2. Two reference frames are shown—left: ecliptic view, looking down from the north. The locations of the Sun, Earth, and both *STEREO* (*A* and *B*) are indicated, and the shaded pink regions indicate the fields of view of the CORs (heavy) and the HIs (light). The straight lines are guidelines for each event, indicating the outermost limits of each as determined by triangulation (near the Sun) and the TH model (farther away); right: front view, showing the location of each event when projected upon the surface of the Sun (Stonyhurst gridlines are shown). The events are labeled, the points represent the location of the end points from the triangulation results and the ellipses show the results from the TH model. The green curves indicate the approximate location of the streamer belt surrounding the heliospheric current sheet, determined by measuring the northern and southern limits of the streamer belt observed in COR2-A and COR2-B.

(An animation and a color version of this figure are available in the online journal.)

P2. These are clearly erroneous, and likely arise from human error in the leading edge measurements or from limitations in measurement due to the relatively narrow fov in solar latitude of the HIs.

Second, we can estimate whether different features are expected to interact with each other. There are only two features that appear to interact: CD1 and D5.

Third, we can estimate the relationship between the location of each event and that of the heliospheric current sheet. We find that all of the disconnection events and puffs are within the streamer belt, and all but one of the CMEs, both filaments and the void cross the belt, but are not entirely enclosed within it (CME2 is entirely enclosed within). The blob B1 appears to occur on the southern streamer belt boundary, although the triangulation results place it within the belt. Finally, we can estimate which events are expected to impact an in situ spacecraft, and the time at which this impact is expected to occur. The results suggest possible candidates for Earth impact include D1, CME1, P1, D2, CME2, and D4; possibilities for *STEREO-A* include D4 and P2; and for *STEREO-B* D1 and CME3A. Table 2 provides the estimated time of arrival of each of these at their respective spacecraft.

Table 2
Those Events Estimated by the TH Model to Either Impact or Pass Closely (within 10°) of the Earth or One of the *STEREO* Spacecraft

Event	Earth	*STEREO-A*	*STEREO-B*
D1	2008 Dec 16 00:21	...	2008 Dec 16 06:27
CME1A	2008 Dec 15 16:20	...	...
CME1B	2008 Dec 16 09:21	...	...
P1	2008 Dec 17 09:10	...	...
D2	2008 Dec 18 19:13	...	...
CME2	2008 Dec 22 20:57	...	...
CME3A	...	...	2008 Dec 29 06:09
D4	2009 Jan 1 12:36	2009 Jan 1 12:11	...
P2	...	2009 Jan 12 17:31	...

Notes. The estimated date and UT time of the arrival are given where appropriate. Those events that are expected to impact the Earth or one of the *STEREO* spacecraft (see Section 6) are highlighted in italic font.

6. IN SITU ANALYSIS

Figure 4 is an elongation-time diagram (a “J-map”; Davies et al. 2009) with all of the events labeled. The J-map not only shows the track produced by the passage of each event but it also provides a time at which the event reaches the elongation of an in situ spacecraft. Recall that the events are optically thin in the white-light images and the nature of Thomson scattering is such that their directions may span a large range of angles from the sky plane (Howard & Tappin 2009; Howard & DeForest 2012b). Although estimations of the impact likelihood and expected arrival time of the events most likely to impact Earth of a *STEREO* spacecraft have been provided in Table 2, our approach in the analysis of the in situ data is to allow for the possibility that every event may have impacted.

The elongation of each in situ spacecraft is marked as a dashed line in Figure 4: *STEREO-B*, 50°; *Advanced Composition Explorer* (*ACE*), 70°; *STEREO-A*, 90°. We measured the time at which each event track reaches the elongation of each spacecraft and then examined the in situ data for signatures at each time interval. We looked for anything out of the ordinary, including notable deviations in magnetic field strength and direction, solar wind plasma properties, energetic particle populations, and ionic abundance variations. We identified possible signatures for six events, but uncertainties in the timing led to some confusion between distinguishing some separate events. Our observations and preliminary analysis are discussed in the sections below.

6.1. CME1A/CME1B (STEREO-B: December 15–17)

CME1 is the same 2008 December CME that is well documented (Davis et al. 2009; Lugaz et al. 2010; Liu et al. 2010; Byrne et al. 2010). As the *Wind* in situ data set has been discussed in many of these papers, we will not revisit it here except to state that a density jump and sheath are followed by a magnetic cloud,

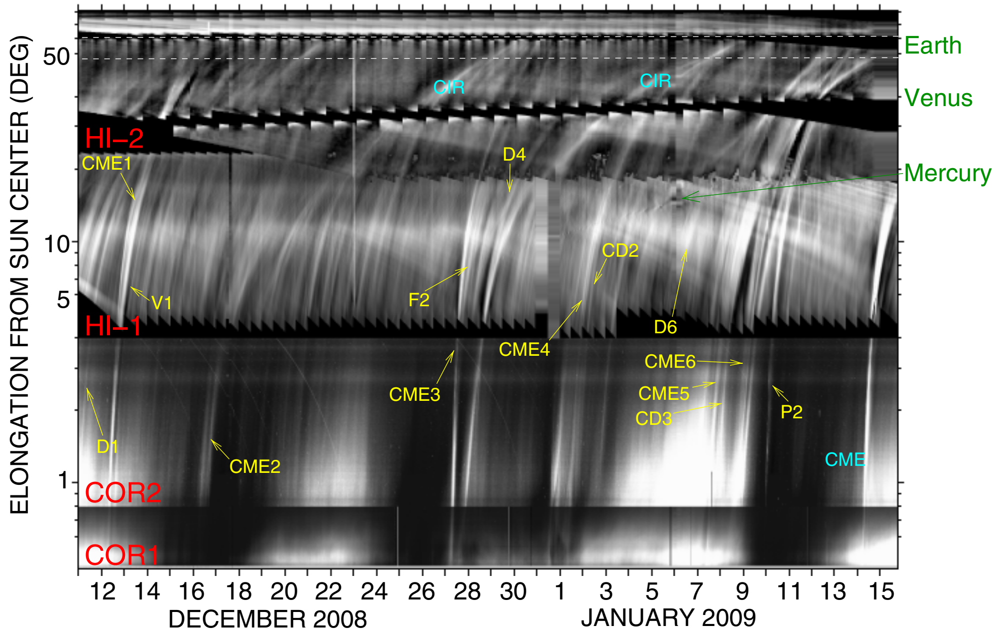

Figure 4. J-map of the ecliptic plane for the entire SECCHI data set December 9 to January 15. The field of view of each instrument is labeled (red), and events have been labeled (yellow) according to Table 1. Only 14 events are shown, as the others did not cross the ecliptic. Mercury, Venus, and Earth are indicated (green, Mercury crosses the ecliptic briefly) at their elongations, and (white) dashed lines indicate the elongations of Earth and *STEREO-B*. Other phenomena of note that were not considered in the present paper, but nonetheless are of interest, are labeled (cyan).

(A color version of this figure is available in the online journal.)

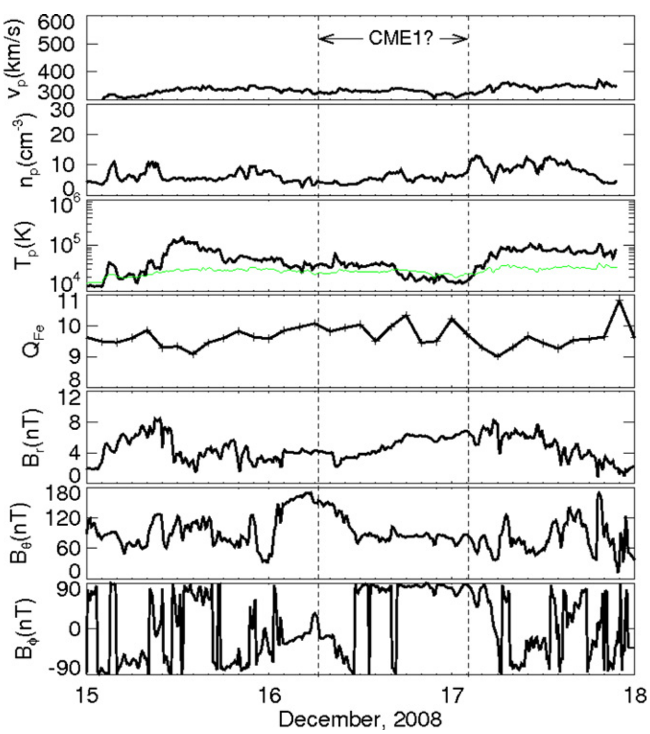

Figure 5. *STEREO-B* in situ PLASTIC and IMPACT data from December 15–18 showing the possible signature of CME1. Plots are shown, from top to bottom: solar wind speed (v_p), density (n_p), temperature (T_p and $T_{\rm exp}$), Q state for Fe ($Q_{\rm Fe}$), and the three components of the magnetic field in polar (B_r, B_θ, B_ϕ) coordinates. The approximate start and end times of the possible CME1 are indicated by the vertical dashed lines.

(A color version of this figure is available in the online journal.)

observed by *Wind* on December 16–17 and the magnetic cloud begins around 04 UT on December 17.

Figure 5 shows *STEREO-B* in situ data for the time period between December 15–18 (see also Figure 2 of Howard & DeForest 2012a). Magnetic field data are shown in spherical polar coordinates. Along with the temperature there is also a $T_{\rm exp}$ parameter, which is the expected temperature based on the solar wind speed. This is an indicator of CMEs as in the ambient solar wind the in situ temperature and $T_{\rm exp}$ are well correlated, while in CMEs the temperature is often anomalously low (Neugebauer & Snyder 1966; Gosling et al. 1973). The ionic charge state $Q_{\rm Fe}$ is also shown: when measured in situ, they are related to the source region temperature and enhanced charge states are common in CMEs, possibly due to flare related heating (Lepri & Zurbuchen 2004; Reinard 2005). Between December 16 at 06 UT and December 17 at 02 UT we observe what appears to be a CME. There is a slight rotation in the magnetic field, indicated by the flattening of B_ϕ and the slight gradient in B_θ components. The total magnetic field is enhanced during this period, though it only reaches a value of about 7 nT which is not much higher than typical ambient solar wind values. The temperature is only slightly lower than expected in the second half of this event and not depressed during the first half. The speed is essentially flat during this period, indicating that this feature is likely moving at or near the solar wind speed. The density remains approximately constant, with perhaps a small density pileup at the end of the event, which is consistent with a slow CME. These features are very weak as are the magnetic cloud signatures, and we suggest that this may possibly be one of the flanks of a flux rope (as also suggested by Howard & DeForest 2012a). One remarkable difference is that the direction of the field rotation is opposite in *STEREO-B* than was observed by *Wind*. This may be the result of attenuation of the flux rope structure along the flank, or that the event observed at *STEREO-B* is different to that observed at *Wind*. The similarity in the temperature data, which has three distinct drops at both *STEREO-B* and *Wind*, suggests that we are likely observing the same large-scale structure in *Wind* and *STEREO-B*. In *STEREO-B* the temperature drops occur on December 15 at 1200, December 16 at 18 UT, and December 17 near 00 UT. At *Wind* we see a similar profile (though

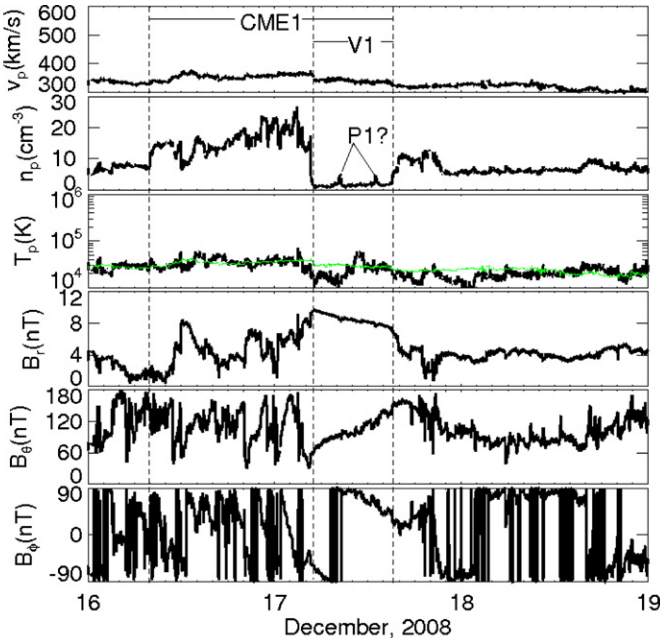

Figure 6. *ACE* in situ SWEPAM and MAG data from December 16 to 19 showing the possible signature of P1. Plots are shown as in Figure 5 with the absence of $Q_{\rm Fe}$. The timing of CME1 and V1 (already identified in other studies) are shown by the vertical dashed lines.

(A color version of this figure is available in the online journal.)

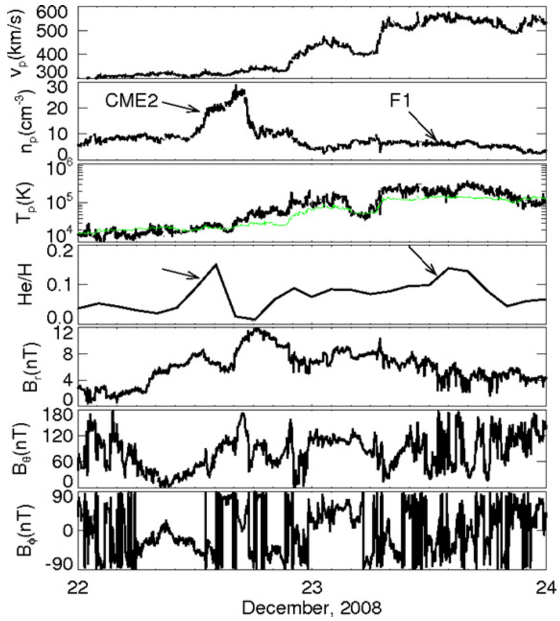

Figure 7. *ACE* in situ data from December 22 to 24 showing possible signatures of CME2 and F1 (labeled). Plots are the same as with Figure 5, except that $Q_{\rm Fe}$ has been replaced with the helium/hydrogen ratio He/H.

(A color version of this figure is available in the online journal.)

with different magnitudes) with temperature drops occurring on December 17 around 04 UT, 11 UT, and 19 UT.

6.2. P1/D2 (ACE: December 16–18)

Figure 6 depicts *ACE* data from December 16 to 19 during the period in which HI-2 observations suggest that CME1A, CME1B as well as the void (V1), a puff (P1), and a disconnection (D2) reach the elongation at which the Earth lies. P1 and D2 both correspond to a predicted arrival time of ∼11 UT on December 17. Variances in the solar wind and feature speed cause the error bars on feature arrival times to possibly be as high as ±4 hr, and so P1 and D2 may arrive anywhere between the beginning and end of the magnetic cloud. Either feature is possible at that location within a magnetic cloud: a puff is likely a density enhancement, which may be part of a CME or may be unrelated, and a disconnection/reconnection event would be expected following a large closed flux region such as a CME.

Gosling et al. (2005) describe an in situ observation of magnetic reconnection, which includes the brief enhancements in density and speed and the anti-correlation of speed and magnetic field components. There is a small peak in density and a magnetic field depression around 0830 and 13 UT on the 17th that would be consistent with a reconnection region; however, the reconnection signature is not present in the speed and magnetic field component data (J. T. Gosling 2011, private communication). This indicates that active reconnection is not occurring there. This result suggests that we are probably not seeing the disconnection region in the in situ data and therefore the observed features at *ACE* are not signatures of D2.

We do, however, observe two density increases, either of which could be caused by the arrival of the puff P1. Given that we know little else about this phenomenon we cannot positively identify it, but the timing of the first density enhancement does match well with the predicted arrival time of P1 at *ACE* (Table 2).

6.3. CME2/F1 (ACE: December 22–23)

Figure 7 shows *ACE* data for the time period from December 22 to 24. The density pileup and speed structure beginning around 12 UT on December 22 are consistent with a relatively fast CME expanding into a surrounding slower ambient solar wind, and while the magnetic field is slightly enhanced, there is no apparent rotation of the field. There is also no temperature depression. Figure 7 also shows helium density from *ACE*/SWICS. At this time *ACE* and *Wind* were 335 Mm from each other. The measured solar wind speed varied between 350 and 500 km s^{-1}, corresponding to a maximum delay of ∼16 minutes. As the helium density is calculated once every 60 minutes, it is impossible for us to correct for this delay. Helium abundance is enhanced slightly during this event, above the 6% threshold commonly used to identify CMEs (Richardson & Cane 2004). Helium increases in the sheath region at the same time as the proton density increases, which is expected. Table 2 predicts that CME2 will impact *ACE* on December 22 at 20:57 UT.

There is a second increase in helium on December 23 at about 16 UT. This second peak is not associated with an increase in proton density and charge state data are not available for this event due to poor statistics (S. T. Lepri 2011, private communication). TH does not predict an impact of F1 with *ACE*, so F1 does not appear in Table 2. TH does predict, however, that F1 will miss *ACE* by only 20° and its closest approach will occur on December 23 at 19:48 UT. This matches well with the timing of the second helium abundance enhancement. Our conclusion therefore is that the CME signature is likely CME2, and the second helium abundance is probably the filament F1.

6.4. CME6 (STEREO-B: January 12–14)

In Figure 8, we see *STEREO-B* observations from 2009 January 12 to 14. A possible CME begins around 12 UT on January 12 with typical magnetic cloud features including a rotating magnetic field and depressed temperature, but no obvious field enhancement. These signatures end around 00 UT

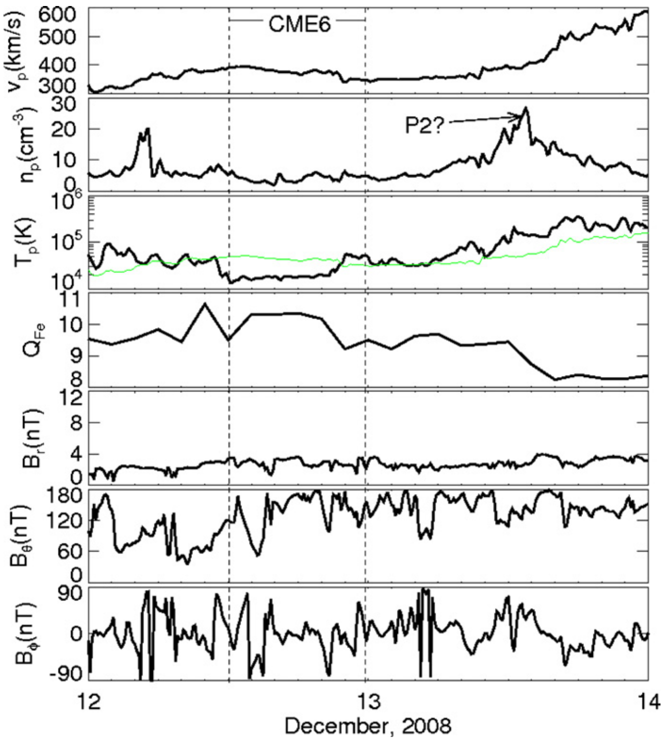

Figure 8. *STEREO-B* in situ data from January 12 to 14 showing the possible signature of CME6 (labeled). Q_{Fe} has been returned. While our analysis suggests that it is probably not the case (see the text for details), we have labeled the possible density enhancement around 13 UT on January 13 as possibly being a signature of P2.

(A color version of this figure is available in the online journal.)

on the 13th. Charge state data are available for this period, and while Q_{Fe} is slightly higher than the surrounding ambient wind, it does not meet the threshold of 12 commonly used (Lepri et al. 2001). There is no speed signature with this event, though a density peak precedes it arriving around 04 UT on the 12th. This suggests that the CME speed probably slightly exceeded the solar wind speed at its origin, but not by a significant amount. The TH results for CME6 have already been identified as erroneous, so we are unable to issue a prediction for its arrival at any spacecraft. Inspection of the HI-2 data reveals an approximate arrival time at 50° elongation at 1300 UT on January 12. Based on the in situ data, we therefore believe that CME6 is likely associated with the *STEREO-B* CME from 06 UT on January 12 to 00 UT on January 13.

Along with CME6, the second puff P2 is also expected to arrive at 50° elongation during this time period. Inspection of the HI-2 data indicates an arrival time of around 01 UT on January 13 (as with CME6, the TH results are unreliable for P2). There is a density enhancement that follows the CME, occurring around 13 UT on the 13th. We feel, however, that the time difference between the arrival of P1 at 50° and that of the density enhancement in *STEREO-B* is too great for the two to be the same event.

7. DISCUSSION

We have described an assortment of transient solar wind phenomena that have been observed by the *STEREO*/SECCHI-A instrument suite during the deep solar minimum of 2008 December to 2009 January. While all of these classes of features have been investigated by previous workers this is the first time that they have been tracked unambiguously through the inner heliosphere. This study has shown not only that many of these phenomena survive and maintain their structure out to 1 AU and beyond, but also that it is possible to trace individual small-scale structures from the Sun to the location of existing in situ probes, and that in situ measurements can then be meaningfully performed on them with some certainty as to the solar origin of the structure being measured. We have identified in situ signatures of four events, which accompany a further two associated with CME1 reported elsewhere.

Along with the observational results, this paper also demonstrates a new capability on data processing and analysis. The SECCHI pipeline (the results of which are shown in Figure 1, and which was developed by DeForest et al. 2011 and refined by DeForest et al. (2012) and Howard & DeForest 2012a), provides the clearest white-light heliospheric image data sets to date. It allows the continuous monitoring of large and small-scale features throughout the heliosphere and enables a direct comparison with in situ density data. The new analysis display shown in Figure 3 shows the results of triangulation and geometry (TH) analysis with respect to the ecliptic plane and the solar disk, to enable a multitude of comparisons to be made. We believe that these developments represent a major milestone of the *STEREO* mission.

7.1. Accounting for Discrepancies between Triangulation and TH

Discrepancies between the three-dimensional location of features via TH versus triangulation highlight the uncertainties that arise from these techniques. Many of these uncertainties are known. The TH model, for example, performs poorly when the measured leading edge does not have a known boundary at one or either end, such as for large CMEs that are measured from only one HI-2 data set (e.g., Tappin & Howard 2009b). Each HI observes roughly one quadrant of the sky so it is not uncommon for large events such as CMEs to extend beyond the associated fov. TH also simplifies the structure of the feature and does not allow for discrepancies in the geometry of the leading edge, such as ripples, dents, and asymmetric distortion. Triangulation is based on the assumption that the measured point is at the same location in three-dimensional space regardless of the observer. Discrepancies arise when this assumption breaks down, which occurs much more commonly than might be expected—as we discuss in the next section. Additionally, measurement error in the location of the leading edge of a feature can be significant and varied, both because of instrumental variations across the full SECCHI field and because of physical effects such as accretion of potentially several times the original mass of a given feature.

7.1.1. Errors Arising from Triangulation

One discrepancy between the triangulation and TH results occurs frequently enough for it to be statistically significant, thereby suggesting that something other than coincidence has affected the results. Leaving aside the 2 events (CME6 and P2) for which TH provided erroneous results and those 8 events that were perfectly aligned in longitude (see Table 1, where $\Phi \pm \Delta\Phi$ cross each other for triangulation and TH), for *all* of the remaining 14 events the triangulation results placed the event further from the Sun–Earth line than the TH results; more than 4 times further for 10 events. This strongly implies that either the TH results are biased toward the Sun–Earth line, or that the triangulation results are biased away from it. We believe that the latter is occurring for reasons given below.

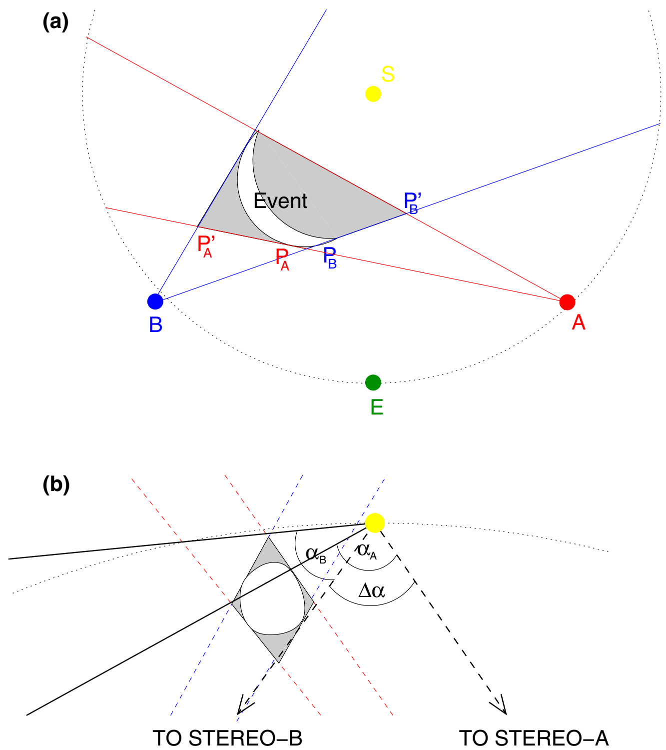

Figure 9. (a) An arbitrary structure viewed from two observers separated in heliographic longitude (modified from de Koning et al. 2009). Here the observers are the *STEREO* spacecraft at their locations on 2009 January 1. The Sun (S), Earth (E), and both *STEREO* (*A* and *B*) are labeled. The structure heads toward *STEREO-B* and its location at a particular time is shown. The leading edges are the lines of sight that meet the CME exactly at a tangent, and these lines are shown from both observers along two sides. The event structure is entirely enclosed within the polygon bound by the cross points between the four lines of sight, shown as the gray shaded area. Because of the optically thin nature of the event, an observer is inclined to identify the location of the leading edge as one of the vertices (P′) rather than its true position (P). This biases our measurement of the location of a CME toward this far edge of the polygon along the line of sight. (b) The geometry required for geometric triangulation calculations, with the longitude α relative to each observer (A and B) and the angular separation between them ($\Delta\alpha$) shown.

(A color version of this figure is available in the online journal.)

The triangulation results were determined using either *STEREO-A* or *B* (depending on which observed the event most clearly) and *Solar and Heliospheric Observatory* (*SOHO*)/LASCO always as the other observer. The triangulation results, therefore, show a possible bias in the direction away from the primary observers.

The problem with triangulation arises from the optically thin nature of the observed transients. Geometric localization is based on the assumption that the same point in three-dimensional space is simultaneously observed by two observers from different locations. However, any measured point along a CME front cannot be accurately localized, partly because transients in the corona are optically thin and partly because they are extended continuous structures and not a collection of packets. We therefore have a tendency to assume the measured point is at the far end of the optically thin structure. The result is a bias toward the end point along the line of sight bound by the volume containing the observed structure.

To illustrate the effect of observer bias on triangulation, consider the situation in Figure 9(a), which is a modified version of Figure 2 of de Koning et al. (2009). There are two lines of sight for each observer, both of which cross the CME at exactly a tangent (i.e., the leading edge). The CME structure is entirely enclosed within a polygon bound by the cross points of the four lines of sight (the gray shaded region). The true locations of a single leading edge on the CME are labeled P_x (x is either A or B). Because of the optically thin nature of the structure, an observer may assume the event lies at the apex of the bounding polygon (i.e., at P'_x) rather than its true position. The magnitude of the distance between P_x and P'_x depends on the structure's location and geometry, but, as shown here, can be large. Hence, as correctly discussed by de Koning et al. (2009), the best we can do with white-light imaging is to place the structure somewhere within the bounding polygon. The geometry required for geometric triangulation becomes that in Figure 9(b), which is meaningless since we can no longer assume at any time that the same point in three-dimensional space is being observed by the two observers. Exceptions include events that are small compared with other distances in the observing geometry (e.g., DeForest et al. 2012), or those that are structured and oriented in a particular way such that the far end of the polygon is very close to the actual point where the line of sight crosses at a tangent to the structure.

The TH results overcome these difficulties of triangulation in two ways: the reconstructions were performed using HI-2A data only; and the model assumes that the event is a complete geometric structure. This is possible when the event is observed across large angles in the sky such as those observed by heliospheric imagers, but it is not possible at small angles such as observed by coronagraphs. At small angles many of the assumptions that simplify the analysis of coronagraph data also remove any three-dimensional information about the observed structures (see Howard 2011). We therefore conclude that except for the two cases where TH is clearly erroneous, whenever there is disagreement between the triangulation and TH results then it is most likely that the TH results are more accurate. As mentioned above, for one-third of the events there was agreement between triangulation and TH.

We conclude with a word of caution against relying too heavily on triangulation results when locating CMEs and other features, and strongly advise against triangulation being used alone to interpret heliospheric imager observations.

The authors thank the SECCHI and HI teams for the kind use of their calibrated data. SECCHI data are produced by a consortium of international groups, including NASA/GSFC (US), RAL (UK), NRL (US), UBHAM (UK), MPS (Germany), CSL (Belgium), and IOTA and IAS (France). A.A.R. acknowledges valuable conversations with T. Mulligan. The work for the present study was supported in part by the NSF/SHINE Competition, Award 0849916, and in part by the NASA Heliophysics program through grant NNX10AC05G. The data analysis for this work made extensive use of the freeware Perl Data Language available at http://pdl.perl.org.

REFERENCES

Byrne, J. P., Maloney, S. A., McAteer, R. T. J., Refojo, J. M., & Gallagher, P. T. 2010, Nature Commun., 1, 74
Davies, J. A., Harrison, R. A., Rouillard, A. P., et al. 2009, Geophys. Res. Lett., 36, L02102
Davis, C. J., Davies, J. A., Lockwood, M., et al. 2008, Geophys. Res. Lett., 36, L08102
DeForest, C. E., Howard, T. A., & McComas, D. J. 2012, ApJ, 745, 36
DeForest, C. E., Howard, T. A., & Tappin, S. J. 2011, ApJ, 738, 103
de Koning, C. A., Pizzo, V. J., & Biesecker, D. A. 2009, Sol. Phys., 256, 167
Eyles, C. J., Harrison, R. A., Davis, C. J., et al. 2009, Sol. Phys., 254, 387

Eyles, C. J., Simnett, G. M., Cooke, M. P., et al. 2003, Sol. Phys., 217, 319
Gosling, J. T., Pizzo, V., & Bame, S. J. 1973, J. Geophys. Res., 78, 2001
Gosling, J. T., Skoug, R. M., McComas, D. J., & Smith, C. W. 2005, J. Geophys. Res., 110, A01107
Harrison, R. A., Davis, C. J., Eyles, C. J., et al. 2008, Sol. Phys., 247, 171
Houminer, Z., & Hewish, A. 1972, Planet. Space Sci., 20, 1703
Howard, R. A., Moses, J. D., Vourlidas, A., et al. 2008, Space Sci. Rev., 136, 67
Howard, T. A. 2011, J. Atmos. Sol. Terr. Phys., 73, 1242
Howard, T. A., & DeForest, C. E. 2012a, ApJ, 746, 64
Howard, T. A., & DeForest, C. E. 2012b, ApJ, 752, 130
Howard, T. A., & Tappin, S. J. 2008, Sol. Phys., 252, 373
Howard, T. A., & Tappin, S. J. 2009, Space Sci. Rev., 147, 31
Howard, T. A., & Tappin, S. J. 2010, Space Weather, 8, S07004
Howard, T. A., Webb, D. F., Tappin, S. J., Mizuno, D. R., & Johnston, J. C. 2006, J. Geophys. Res., 111, A04105
Illing, R. M. E., & Hundhausen, A. J. 1985, J. Geophys. Res., 90, 275
Lepri, S. T., Zurbuchen, T. H., Fisk, L. A., et al. 2001, J. Geophys. Res., 106, 29231
Lepri, S. T., & Zurbuchen, T. H. 2004, J. Geophys. Res., 109, A01112
Linker, J. A., Van Hoven, G., & McComas, D. J. 1992, J. Geophys. Res., 97, 13733
Liu, Y., Davies, J. A., Luhmann, J. G., et al. 2010, ApJ, 710, L82
Lugaz, N., Hernandez-Charpak, J. N., Roussev, I. I., et al. 2010, ApJ, 715, 493
McComas, D. J., Gosling, J. T., & Phillips, J. L. 1992, J. Geophys. Res., 97, 171
McComas, D. J., Phillips, J. L., Hundhausen, A. J., & Burkepile, J. T. 1991, Geophys. Res. Lett., 18, 73
Möstl, C., Temmer, M., Rollett, T., et al. 2010, Geophys. Res. Lett., 37, L24103
Neugebauer, M., & Snyder, C. W. 1966, J. Geophys. Res., 71, 4469
Reinard, A. A. 2005, ApJ, 620, 501
Richardson, I. G., & Cane, H. V. 2004, J. Geophys. Res., 109, A09104
Rouillard, A. P., Davies, J. A., Forsyth, R. J., et al. 2008, Geophys. Res. Lett., 35, L10110
Rouillard, A. P., Davies, J. A., Lavraud, B., et al. 2010, J. Geophys. Res., 115, A04103
Russell, C. T., Luhmann, J. G., & Jian, L. K. 2010, Rev. Geophys., 48, RG2004
Sheeley, N. R., Jr., Herbst, A. D., Palatchi, C. A., et al. 2008, ApJ, 675, 853
Sheeley, N. R., Jr., Lee, D. D.-H., Casto, K. P., Wang, Y.-M., & Rich, N. B. 2009, ApJ, 694, 1471
Sheeley, N. R., Jr., & Rouillard, A. P. 2010, ApJ, 715, 300
Sheeley, N. R., Jr., Wang, Y.-M., Hawley, S. H., et al. 1997, ApJ, 494, 472
Tappin, S. J., Buffington, A., Cooke, M. P., et al. 2004, Geophys. Res. Lett., 31, L02802
Tappin, S. J., & Howard, T. A. 2009a, ApJ, 702, 862
Tappin, S. J., & Howard, T. A. 2009b, Space Sci Rev., 147, 55
Webb, D. F., Howard, T. A., Fry, C. D., et al. 2008, Sol. Phys., 256, 239
Zita, E., Smith, C., Ballou, C., et al. 2010, Proc. Am. Phys. Soc., 12th Ann. Meet. Abstract H1.005